*International Journal of Engineering & Technology*, 7 (2.25) (2018) 56-63

International Journal of Engineering & Technology

*Website: www.sciencepubco.com/index.php/IJET*

***Research paper***

# An approach to automated retinal layer segmentation in SDOCT images

**Mohandass G [1] *, Hari Krishnan G [2], Hemalatha R J [3],**

[1] *Bahrain Training Institute, Behrain*
[2] *Sree Vidyanikethan Engineering College, Tirupati, Andhra Pradesh, India*
[3] *Vels Institute of cience,Technology and Advanced studies (VISTAS),Chennai, India*
**Corresponding author E-mail: g.mohandass@gmail.com*

## Abstract

The optical coherence tomography (OCT) imaging technique is a precise and well-known approach to the diagnosis of retinal layers. The pathological changes in the retina challenge the accuracy of computational segmentation approaches in the evaluation and identification of defects in the boundary layer. The layer segmentations and boundary detections are distorted by noise in the computation. In this work, we propose a fully automated segmentation algorithm using a denoising technique called the Boisterous Obscure Ratio (BOR) for human and mammal retina. First, the BOR is derived using noise detection, i.e., from the Robust Outlyingness Ratio (ROR). It is then applied to edge and layer detection using a gradient-based deformable contour model. Second, the image is vectorised. In this method, a cluster and column intensity grid is applied to identify and determine the unsegmented layers. Using the layer intensity and a region growth seed point algorithm, segmentation of the prominent layers is achieved. The automatic BOR method is an image segmentation process that determines the eight layers in retinal spectral domain optical coherence tomography images. The highlight of the BOR method is that the results produced are accurate, highly substantial, and effective, although time consuming.

***Keywords***: *Image Analysis; Noise in Imaging Systems; Image Detection Systems; Transforms; Computational Imaging; Optical Coherence Tomography; Ophthalmology.*

## 1. Introduction

Optical coherence tomography (OCT) is an imaging technique to analyse retinal layers [1–2]. Segmentation is a challenging task in OCT retinal images.

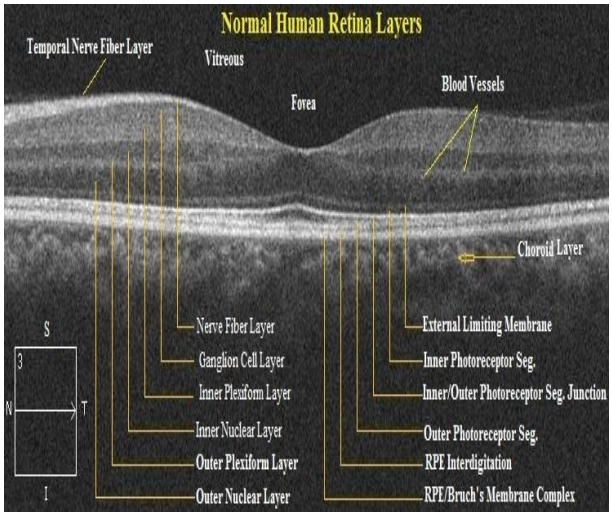


**Fig. 1:** Cross-Section Image of the Retinal Layers.

Commercial OCT devices measure the nerve fibre layer and total retinal thickness [3]. The retina is a multilayer structure (of ten layers). Figure 1 show a cross section of Spectral Domain Optical Coherence Tomography (SDOCT) images. The anatomical structure of the retina consists of the retinal pigment epithelium (RPE), inner photo receptor layer (I-PRL), inner/outer photo receptor layer (IO-PRL), outer photo receptor layer (O-PRL), external (or outer) limiting membrane (ELM or OLM), outer nuclear layer (ONL), outer plexiform layer (OPL), inner nuclear layer (INL), inner plexiform layer (IPL), ganglion cell layer (GCL), and internal limited membrane (ILM)/nerve fibre layer (NFL). The photoreceptor layer is a very complex layer, and the primary information is attained by manual segmentation [4–5].

In this paper, a fully automatic segmentation approach is presented using a statistical outlier ratio. This efficient method extracts layer features and reduces analysis time. In this study, we focus on SDOCT retinal layer images. The thickness of the retinal layer and position of the boundaries determine the disease diagnosed. In denoising research, a median filter is often proposed [6–7]. Fernandez et al. [8] proposed the active counter, which is the most traditional segmentation method and uses a two-step kernel optimization technique. Yazdanpanah et al. [9] introduced the modified active contour for a multiphase framework in SDOCT data. In addition, the algorithm was robust and avoids initial training procedure. Regardless, active contour algorithms are resistance to 2D noise and in better accuracy. Active contour methods were first proposed by Fernandez and modified by Yazdanpanah. Time complexity and exact error reports are not report for future investigation. In 2008, Mayer et al. [10], calculated the RNFL thickness in circular SDOCT B-Scan using fuzzy C-means clustering techniques. These types of approach have been overtaken by graph theory methods in terms of accuracy and time. Again in 2010, Mayer et al. [11] used a gradient

and local smoothing function for extracting segments from SDOCT images on 132 scans from normal subjects and 72 scans from glaucoma patients. A mean absolute error per A-Scan of 3.6 mm on healthy eyes and 2.9 mm was achieved in glaucomatous eyes. This proved the reliable tool for glaucoma diagnosis in OCT B-Scans. Ghorbel et al. [12] segmented eight retinal layers in a Heidelberg Spectralis SDOCT image using global segmentation algorithms such as active contours and Markov random fields. In addition, a Kalman filter was designed to detect and segment the photoreceptor layers. The algorithm was experimented on a set of 700 retinal images acquired in-vivo from healthy subjects. This method is limited in its scope and impact. Vermeer et al. [13] reduced the processing time in 3D OCT segmentation using smoothing, SVM, and by training an error classifier with accuracy results. Here, parts of OCT scans were manually segmented for learning the process. RMS errors of the retina (top and bottom) were between 4 and 6 µm. Similarly, errors for intra-retinal interfaces were between 6 and 15 µm. Yang et al. [14] method identified nine retinal layers using Canny edges and the axial graph intensity gradient derived from the Canny edge maps. This algorithm works for low intensity and low contrast OCT images. For each boundary, the intra class correlation coefficient was above 0.94, variation of the mean coefficient was less than 7.4%, and the mean standard deviation was less than 2.8 µm. This method was able to segment without pre extraction procedure in a very short time without degrading the accuracy. Abramoff et al. [15] proposed a combination of 3D graph search and a voxel k-Nearest Neighbors (k-NN) classifier for segmenting the optic nerve head (ONH) rim and cup in SDOCT data from 34 glaucoma patients. This basic study showed a high correlation between segmentation results of the ONH rim and cup from SDOCT images. They incorporate, the correlation of algorithm with planimetry results obtained by three independent glaucoma experts on the same was 0.90, 0.87, and 0.93, respectively. Lee et al. [16] presented an improved and fully automatic method using graph search and k-NN classifiers to segment the optic nerve head (ONH) rim and cup on 27 SDOCT scans from 14 glaucoma patients. They reported unsigned error for the neuroretinal rim was 2.04 ± 0.86 pixels (0.061 ± 0.026 mm) and for the optic disc cup was 2.52 ± 0.87 pixels (0.076 ± 0.026 mm). Quellec et al. [17] presented a method for identification of fluid-filled regions in SD-OCT images from AMD patients. This approach also used a machine learning method with multiscale 3D graph search techniques to segment ten layers. The segmented layers were characterized by 3D textural features and their thickness. They reported mean unsigned surface positioning errors were less than 6 µm. Chiu et al. [18] proposed a graph theory and a dynamic programming method that reduces the processing time. This methodology was able to address sources of instability such as vessel hypo-reflectivity, the merging of fovea layers, the presence of pathology and uneven tissue reflectivity. Interestingly, the method incorporates an automatic initialization that eliminates the need for manual endpoint selection. Kafieh et al. [19] proposed method detected 12 retinal boundaries using coarse grained diffusion map. Diffusion map was applied on 2D and 3D OCT datasets. This relied on regional image texture and the pre extraction of vessel locations was unnecessary in this method. The method was experimented on 23 datasets from two patient groups (13 datasets, 3D-OCT obtained from healthy eyes and 10 datasets, 3D-OCT data from patients diagnosed with glaucoma). They reported that mean unsigned border positioning errors (mean ± SD) was 8.52 ± 3.13 mm and 7.56 ± 2.95 mm for the 2D and 3D approaches, respectively.

Evaluation of the appropriate algorithm are based on high accuracy in detecting the retinal boundaries, fully automated, reduce computational time, denoising technique, report on various pathologies with grades and validate the procedure to ensure true-worthy result [20].

Speckle noise in the OCT images disrupts the good formation of segments in retinal layers [21–22]. Many segmentation procedures first use denoising algorithms [23–26], and an effective method is needed. To address this issue, a segmentation method is derived in conjunction with a denoising method to improve the efficiency of the algorithm. To achieve this objective, we propose the Boisterous Obscure Ratio (BOR) segmentation method. BOR is derived from the denoising detection technique, Robust Outlyingness Ratio (ROR) [27]. Additionally, contour transformation and edge detection, layer boundary representation, automatic segmentation using image vectorization, gradient generation, and feature-relative mapping layer methods are used on the image.

## 2. Algorithms and implementations

The sequential approach to segmenting OCT images is explained in this section. Figure 2 shows the general block diagram of the algorithm.

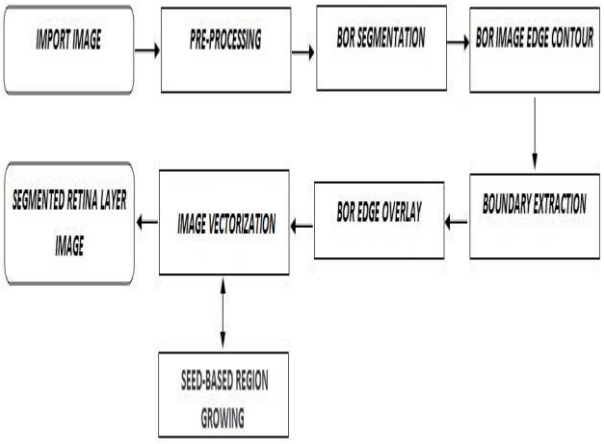


**Fig. 2:** Generalized Block Diagram of the Proposed Method.

### 2.1. BOR segmentation of the retinal layer

In this process, the BOR measures the impulse in each pixel and assigns an impulse value called the BOR value. The term "impulse" refers to a sudden change in pixel value relative to a group of pixels. The pixels are then grouped and segmented. This method assigns values to pixels by taking the median of the image to be segmented. The BOR method uses a threshold value of 0.6713. This value is obtained from standard normal random variables. The BOR segmentation algorithm is given below.

#### 2.1.1 .Algorithm for BOR segmentation

The image that is to be processed is selected (Figure 3(a)). Let A be the selected image. The median of A is calculated and stored in variable Med, i.e., Med = median (A). The median value of A is then subtracted from A and its absolute value is stored in Sub_A, i.e.

$$\text{Sub\_A} = |(A - \text{Med})| \quad (1)$$

After finding the difference between the original image and Med, the median of that particular output becomes the median absolute derivative (MAD), i.e.

$$\text{MAD} = \text{Median (Sub\_A1)} \quad (2)$$

Next, MAD is divided by coefficient C, which is the sample median of the standard normal random variables. The normalized median absolute deviation (MADN) is as follows:

$$\text{MADN}(y) = \text{MAD}(y) / C \quad (3)$$

Thanks to robust statistical theory, we set C to 0.6457 [28]. Here, y is the vector representation of the data.

$$\text{MADN}(y) = \text{MAD}(y) / 0.6457 \quad (4)$$

Finally, the BOR matrix of the pixel $y_{i,j}$ can be obtained by

$$BOR\ (y_{i,j}) = |(A - Med)/\ [MADN(y)]| \quad (5)$$

The unique values U in the BOR value matrix are obtained and sorted in ascending order. The sorted unique values are split into n equal-sized groups. Here, we chose n to be eight, because this value works well for retinal images. For example, in a 200 × 200 × 3 image, we have 120,000 pixels. After applying the BOR method, each pixel will have a BOR value. The unique values from all the BOR values are determined and sorted. Consider the case where there are 8,000 unique values. These 8,000 unique values are grouped into eight groups so that the total number of unique BOR values in each group is 1,000. Each segmented group is assigned a unique colour to represent that particular group. The values of the group are searched for in the BOR matrix and replaced with the corresponding colour. The same process is repeated for the remaining groups. Thus, the final BOR matrix with the substituted colours is the segmented retinal image.

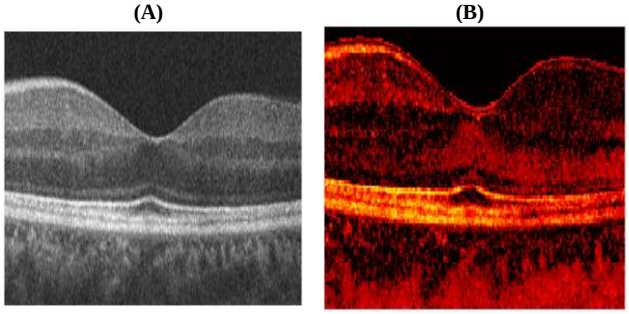


**Fig. 3:** (A) Original Retinal SDOCT Image and (B) Output of the BOR Segmentation Algorithm

Figure 3(b) shows the output of a retinal image after BOR segmentation. In this image, the layer descriptions are indicated by the red composites. The segmented layers are the retinal nerve fibre layers: GCL + IPL, INL, and OPL + ONL. The RPE and photoreceptor layer are also segmented.

## 2.2. Contour transformation and edge detection

Next, a contour transform is applied to the BOR segmented image to identify the frequency variations and intensity variations [29–32]. It is performed by the following steps.

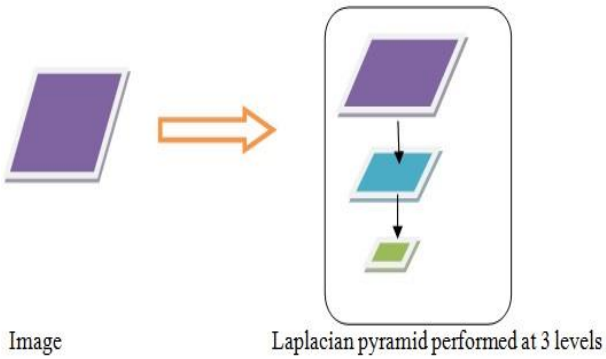


**Fig. 4:** Laplacian Pyramid.

First, the image is processed using a Laplacian pyramid [33]. The size of the image is reduced by half when the filter is first applied. Similarly, the output of the first level is reduced by half when Laplacian filtering is performed again.

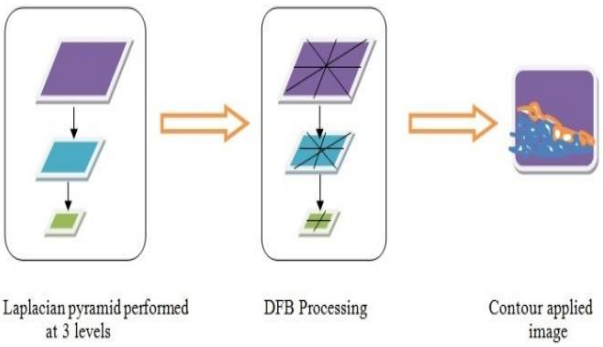


**Fig. 5:** DFB.

Second, each level of the Laplacian pyramid is input for the next level in a method called a directional filter bank (DFB) [34–35]. The DFB is formed using two blocks. The first block is a two-channel quincunx filter bank with fan filters that divides a 2-D spectrum into two directions: horizontal and vertical. The second block of the DFB is a shearing operator that simply reorders the image samples. When each level of the Laplacian pyramid is filtered by the DFB, frequency variations are obtained. These frequency variations by level are combined together and thus form a contour plot.

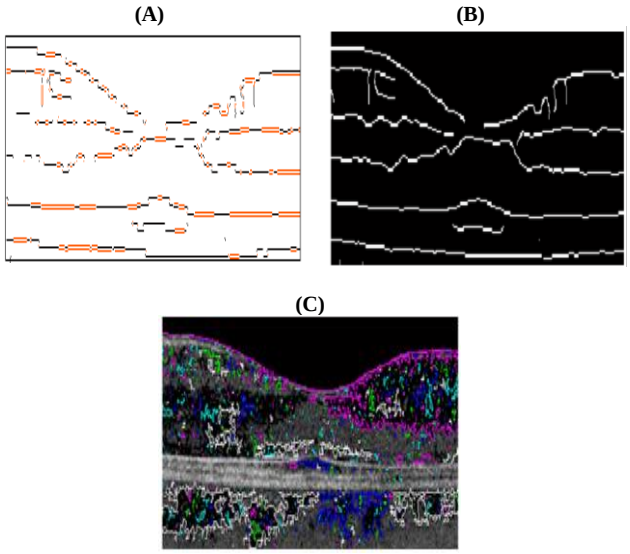


**Fig. 6:** Contour Transform and Edge Detection: (A) Contour Plot of the Image, (B) Image Edges, and (C) Pixel Intensities Overlaid (BOR Lining).

In Figure 6(a), the NFL, inner/outer photo receptor layers, and RPE/Bruch's membrane are clear. Partial and discontinuous edges are formed in the GCL, plexiform layer (inner and outer), and the nuclear layer (inner and outer). Third, to detect the edges, a Canny operator is applied (Figure 6(b)). Edge detection is applied to the BOR segmented image to classify the retinal layers [36]. Figure 6(c), shows the output with the segmented BOR overlaid. This output does not identify any layers and the different intensity values are indicated by various colours. This image is called a BOR lining.

## 2.3. Representing boundaries for layers

Boundaries are formed by highlighting the edges [37]. In the image, the BOR boundaries are formed by two outputs: the edge-detected output of the BOR and the contour plot of the BOR image.

### 2.3.1. Representing boundaries using edges

The edge-detected output is overlaid on the BOR images to highlight the layer boundaries. To overlap, first we collect the row and column positions of the pixels with a certain value. Next, we plot those positions on the BOR image using different colours in the output image. The computational approach is given as follows:

$$\beta(\Delta(x) = \varepsilon(\varphi(\Delta(x)) \quad (6)$$

Where x is the input image, β(x) denotes the boundaries in x, ε(x) denotes the positions of image x, and φ(x) is the edge image of x.

### 2.3.2. Representing boundaries using contours

The contour plot is overlaid with the BOR image [38]. It looks clumsy and the layers are not clear. To address this, the edges of the contour plots are used to segregate the layers along with the contour frequencies. Thus, the edges are overlaid on the BOR image to segment the layers. This concept is expressed mathematically as follows:

$$\beta(\Delta(x) = \varepsilon(\varphi\gamma(\Delta(x)) \quad (7)$$

Where x is the input image, β(x) denotes the boundaries of x, ε(x) denotes the positions of image x, φ(x) is the edge image of x, and γ(x) denotes the contours of x.

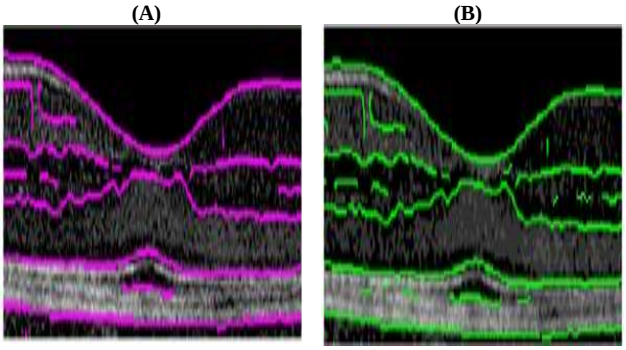


**Fig. 7:** Image Representing the Boundaries of the BOR Segments Based on (A) an Edge Image and (B) A Contour Image.

Figure 7(a) shows the output of edge-based BOR segmentation. In this image, the RPE and photoreceptor layer with its external limiting membrane are identified as a single complex layer. Here, the RNFL and ONL boundary lines are segmented. The IPL boundary is partially formed. Figure 7(b) shows the contour-based BOR segmentation. The result is similar except for the partial formation of the IPL and GCL. The BOR algorithm successfully segments four prominent layers: RPE, I/O-PRL, ONL, and NFL. To extend the identification of partially formed layers, an image vectorisation procedure is used.

## 2.4. Image vectorisation and segmentation

The image after the edge contours are found portrays layers that are not continuously connected. To correct the continuities of the layers, we use the following methods: layer clustering, grid, seed growing, and image vectorisation for layer tracking in a sequential segmentation approach [39]. First, we apply an adaptive noise reduction filter to smooth the image and identify the fine layers in the image. This is to avoid the intersection of detected layers caused by noise. The basic automatic segmentation procedure begins with a simple "connectivity-based segmentation" [40]. Initially, the input image is converted to a grey scale image and divided into 3 × 3 windows. Next, the algorithm checks whether the pixels in the window are of one value. If this is true, a pilot binary mask is formed by thresholding the edge-enhanced image to generate a mask with respect to direction.

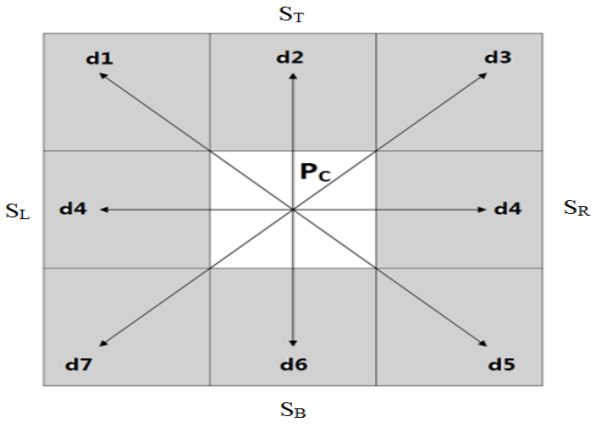


**Fig. 8:** Eight Discrete Directions in a 3 × 3 Neighbourhood.

Here, we use eight discrete directions (d1, d2... d8) with respect to sides ($S_T$, $S_B$, $S_L$, $S_R$), and centre value $P_C$, as shown in Figure 8. Finally, the direct pilot estimate of the retinal layer identifies new locations of x (x = $P_{C1}$, $P_{C2}$ ...) in the search regions in order to merge disconnect layers. Computation is repeated for several iterations until the layers are continuous. The results are shown in Figure 9. From the results, we identified some progress in determining the layers. Hence, we plan to improve the method in future in terms of time and accuracy.

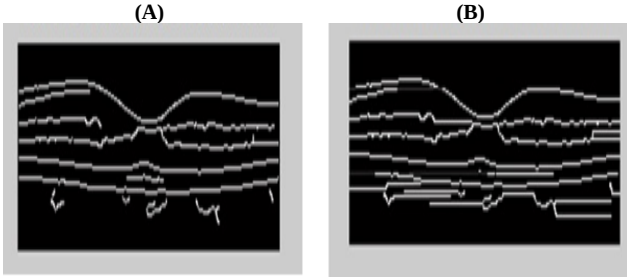


**Fig. 9:** Results of Connectivity-Based Segmentation: (A) Grey Scale Image of BOR-Segmented Output Processed By an Adaptive Noise Reduction Filter and (B) Results after the Connectivity Procedure.

There are two major causes of the error that occurred in the automatic method. One is that if there is little deviation in the selected point, the tracking cannot follow along the direction of the layer. The other is that automatic layer tracing fails if cartographic features meet on the same pixel.

We identified that correct guidance of the pixels is required. To address this, traditional k-means clustering was applied to the image. This method was chosen because it is an unsupervised learning algorithm with fast and accurate grouping of similar pixel intensities. Based on the results of k-means clustering, the disconnected layers are validated by grouping the cluster values according to group size. With respect to automatic performance, k-means clustering and direction seed growing are more suitable, irrespective of weight changes in the pixels, because they are adaptive segmentation methods [41]. By k-means clustering, the disconnected layer and its corner point are determined.

Given the quality of the image, very small clusters can be formed, especially below the chloride layer in the retinal pathology OCT images. To identify clusters in the chloride and discontinuous layers, we applied a grid to the image. A grid is depicted in the cluster image. The retinal image is divided into a smaller rectangular row- and column-wise grid structure. Using this approach, the method can estimate pixel clusters corresponding to hyper-reflective layer regions using a column-wise intensity profiling technique. Using clustering and grid intensity values, the corner point is identified using the Harris corner detector. First, layer identification depends on clusters of bright pixels, particularly corner pixels on the edges. These corner points detected by the grid are next examined to determine if they are corner points in layers. We performed a two-way verification to identify the correct coordination point such that two

points match to one pixel. In future processing, we use conditions to identify layers. In the first condition, pixels formed in the direction of vertical clusters with higher means are dropped. The second condition is the direction of similarly weighted detection pixels values with respect to the layer cluster values. The third condition is that the best way to detect seed growth is by different intensity values that correspond to the respective retinal layers. However, detection using this approach is subject to error and pseudo-pixel identification. To overcome this error, seed growing is applied to the image.

In this approach, the pixels connected in a group form a tentative assignment of the retinal layer. This eliminates and removes the unwanted layers. The intensity of the neighbouring pixels of the initial "seed points" determines whether these neighbours should be added to the region. The threshold is the maximum value of the neighbour pixel that satisfies the conditions. Suppose the image pixel has intensity value $I_I$, the neighbouring pixel intensity value is $I_{NI}$, and the intensity of the threshold values $T_{IN}$. The threshold condition for region growing is as follows:

$$\left\| I_I - I_{NI} \right\| \le T_{IN} \tag{8}$$

The next stage of automatic segmentation relies on the pilot estimate of the retinal layer based on the direction of region growing from the seed point with respect to pixel intensity [42]. Here, using the corresponding pixel points, discontinuous layers are linked by the corresponding threshold pixel values of the layers determined by seed growing techniques by connecting two corner points. From corner point C1, the initial layer is the pilot estimate of the retinal layer using region growing from the seed point that searches for end point C2. Using this approach, unsegmented layers are determined using seed points in the grey scale image.

The correct pixel is identified by the following strategies. First, the grey scale difference between the pixels must be low. Second, equal intensity values are identified. The third strategy is based on the direction of the weight of similar pixel values to the centre seed point. Fourth, each layer has a different intensity value to detect the true seed growth. However, a new seed pixel may still be an error or pseudo pixel.

To overcome this possibility, the following techniques are used. First, the average value of the cluster is calculated and used to grow the seed centre. To accurately search for layers, the lower pixels are added to the cluster. This results in more accurate layers.

This generates a one-to-one mapping of the pixels in the set to form the layer. This is repeated until the other corner point of the layer is found. This operation is repeated to track the segmented layer until an endpoint or an intersection is met. The endpoint may be the intersection between different linear features or noise. Thus, retinal layers are segmented using the traditional gradient feature related mapping and colour layers are generated.

## 3. Results and analysis

The outputs of various automatic segmentations are shown in Figures 10–12. The results show the correct identification of eight layers. The images are processed and a comparative analysis was performed using MATLAB R2014a with a system configured with an Intel Core i5 CPU M 80 at 2.6 GHz, 4.00 GB of RAM, and a 64-bit operating system. The segmentation procedure was computed and analysed using the original retinal SDOCT image of Figure 3(a). This was acquired from a Cirrus HD SDOCT (Carl Zeiss, Meditec Inc, Dublin, CA), software version 5.1.1.4. All the pathological and normal human retinal images used for the study were acquired using this instrument.

Figures 10(a)–(c) below show the results of automatic BOR segmented outputs from retinal SDOCT images of normal and healthy eyes. In non-standardization image condition, average of eight layers is detected. In Figure 10(b) and 10(d), additionally IPL layer is segmented. Figure 10(d) is the output image of a blurred retinal image. Because the BOR algorithm is derived from impulse noise detection, it has a high level of accuracy and effective results for noisy images as well.

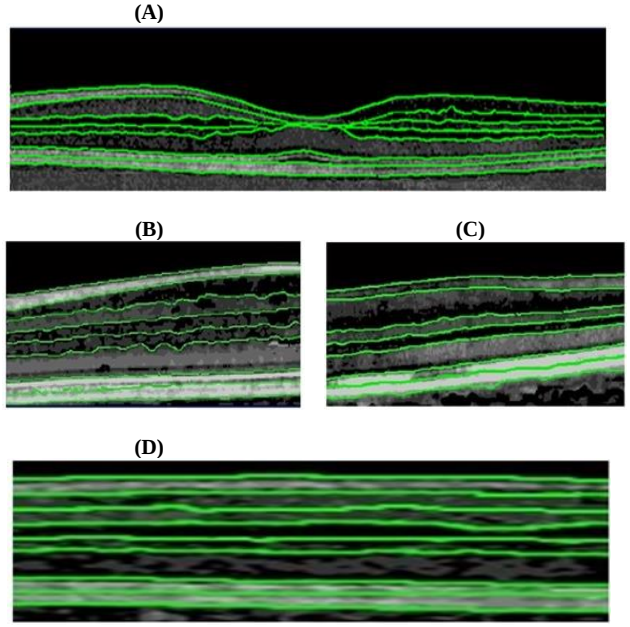


**Fig. 10:** Automatic BOR-Segmented OCT Images of Normal Retinas.

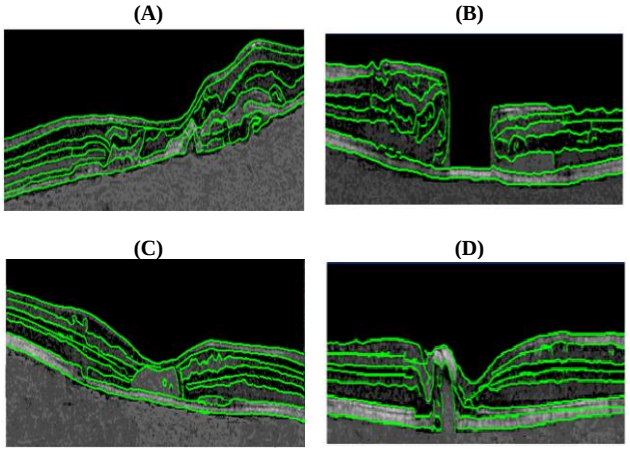


**Fig. 11:** Automatic BOR-Segmented Pathological Retinal OCT Images (A) CNVM, (B) FTMH, (C) ME, and (D) PR.

The automatic BOR segmentations of pathology images are shown in Figure 11 for (a) Choroidal Neovascular Membrane (CNVM), (b) Full-Thickness Macular Hole (FTMH), (c) Macular Edema (ME), and (d) Pigment Plaque (PR). In disease images, these layers are affected. Hence, some unusual and abnormal layers are formed. These outputs represent the major advantage of this algorithm for layer formation in pathology images [43–46].

However, broken lines are the influence of pathological effects in image pixels intensity level. Broken line segmented regression key attributes of multivariate independent pixel data separate by the pathologies clustered in classified pixels non-fit of the wide variation in nonlinear intensity values. These outputs represent the major advantage of this algorithm for layer formation in pathologies image with limits.

The BOR automatic algorithm was also applied to other mammal retina OCT images. The images were acquired using, Bioptigen Envisu R-Class SDOIS (Bioptigen, Inc.; Durham, NC). The results are shown in Figure 12 for dog, mouse, and rabbit normal retina. These are sample image results of major retinal layer formation. There are major differences in axial length, anatomy, and physiology function in humans and mammals [47–50]. In Figure 12(c), the segmentation is laid over the anatomical structure.

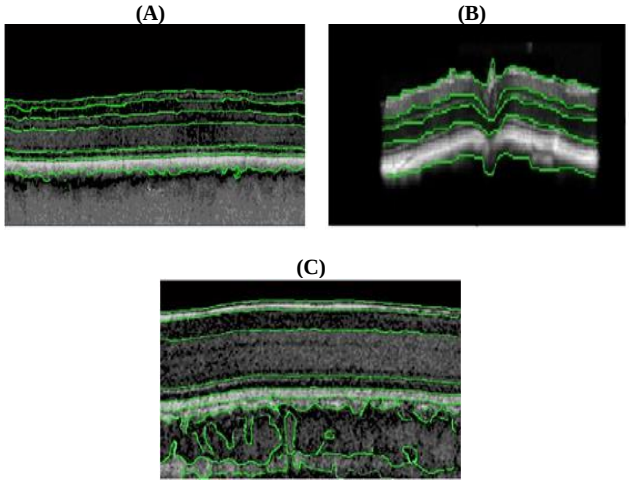


**Fig. 12:** Automatic Segmentation in Animal Retinas: (A) Dog, (B) Mouse, and (C) Rabbit.

**Table 1:** Time Consumed By the Automatic BOR Segmentation Algorithm.

| Sl.No | Name of the image | Time Consumed (s) |
|---|---|---|
| 1. | Normal Retinal SDOCT Image | 2.968 |
| 2. | Choroidal Neovascular Membrane (CNVM) | 4.035 |
| 3. | Full Thickness Macular Hole (FTMH) | 3.575 |
| 4. | Macular Edema (ME) | 4.024 |
| 5. | Pigment Plaque | 3.290 |

Execution times are shown in Table 1, where the normal retinal SDOCT Image time is the average time for BOR segmentation of all the images in Figure 10. In this experiment, 123 original retinal SDOCT images and 92 pathological SDOCT images were analysed. For a total of 215 images, the average time required to automatically segment the image was 5.342 seconds per image. The method proposed here is fast and can automatically segment eight layers. In more sophisticated algorithms, speed is a challenging criterion, and this is achieved in the automatic BOR procedure. Here, the composite result images with green boundaries showed to achieve the objective of a good result in drastically reduce computation time.

In this research, full-fledged correct layer identification was the major objective, and less significance was given to detecting the number of layers. Using the BOR methods, five layers were identified effectively and accurately in all the analysed images. The average time taken for this BOR algorithm was 3.374 seconds per image. Using this automatic method, the majority of the layers were formed, with the exception of the hyper-reflective intra-retinal layers.

Clinically experienced and trained expert human graders evaluation is taken as a high priority for qualitative analysis in the consensus of delineated the retinal layers. Trained expert graders were from Regional Institute of Ophthalmology and Government Ophthalmic Hospital, Chennai. The eight output layers were manually traced by three trained expert grader. Each expertise exhibits their own approach of direction in tracing of consistent layer boundaries either above or below from the actual boundary in respective sequential layers of constant distance.

By the quantitative report of expert graders evaluation, our method have accomplished well by obtaining good metric average values by having better accuracy value of 98.35%. Similarly for the pathological images have the good result of about 92.83%. More deviation is found especially in highly defective pathological grade images. Ultimately, the quality of the image has a directly proportional impact on the excellence of the results using this method. The standardization of images is a very important task [51–53].

We note that layer validation and statistical proof of our algorithm for normal and pathology images is outside the scope of this preliminary paper. However, they will be fully addressed in our future publications. Moreover, layer identification in the pathology images seems to be unusual and required to upgrade the color independent of different retinal layers with minimized computation time, which will be investigated in future work.

The aim of this paper is to produce a clear impression of the development of a new retinal layer detection algorithm. Initially, in this work, no objective was set to quantitatively detect layers, instead, the goal was form exact layers. Finally, in this research, we detected the RPE, O-PRL, I/O-PRL, ONL, OPL, INL, GCL-IPL, and NFL. The automatic BOR algorithm has the added ability to segment the retinal OCT images of different mammalian species.

## 4. Conclusion

A retinal OCT image is an inhomogeneous, complex structure. The segmentation of OCT images and the detection of retinal layers was computed using BOR methods. Because of noise and its distribution, the precise formation of a retinal layer by computational methods is unachievable. Hence, the ROR technique was proposed to detect noise. Additionally, the adaptive segmentation and noise removal algorithm with clustering eliminates disconnected and unwanted layers. BOR was derived using denoising techniques and includes edge detection and an image contour model. This BOR segmentation procedure detects eight retinal layers. BOR can be used to accurately and qualitatively detect layers with intelligent and expert system algorithms. In this study, the method plays a very important role in the result. This is because the qualities of an image determine the number of layers identified. Retinal OCT images from two different commercial instruments were used to analyse both human and animal retinas. This work expanded on the different manufacturing methods of OCT images. Even though, quantitative report of expert graders evaluation is 98.35% and 92.83% for normal retina and pathologies retinal segmentation respectively, statistical validation of the detected layers will be addressed in future research with different images.

## 5. Competing interests

The authors declare that they have no competing interests.

## Acknowledgement

Mr. Mohandass G. would like to thank Mr. C. Raja, (Thanjure) for providing OCT images from Aravind Eye Hospital, Pondicherry. Special thanks to Mr. C. Sathish Gunasekaran (Mogappair East) and the Director of RIO-GOH, Egmore, in support of OCT images. Special thanks to Mr. T. Vishnu (Coimbatore) and Dr. R. Ravanan, (Presidency College) for their helpful contributions during the development of this study. This research received no specific grant from any funding agency in the public, commercial, or not-for-profit sectors.

## References

[1] D. Huang, E. A. Swanson, C. P. Lin, J. S. Schuman, W. G. Stinson, W. Chang, M. R. Hee, T. Flotte, K. Gregory,C. A. Puliafito, Optical coherence tomography, Science, Vol.254, No.5035, (1991)1178–1181.

[2] J. G. Fujimoto, W. Drexler, J. S. Schuman, and C. K. Hitzenberger, “Optical Coherence Tomography (OCT) in ophthalmology: introduction,” Opt. Express, vol.17, No.5, 3978–3979.

[3] Nazli Demirkaya, Hille W. van Dijk, Sanne M. van Schuppen, Michael D. Abr`amoff, Mona K. Garvin, Milan Sonka, Reinier O. Schlingemann, and Frank D. Verbraak, "Effect of Age on Individual Retinal Layer Thickness in Normal Eyes as Measured With Spectral-Domain Optical Coherence Tomography", Invest. Ophthalmol. Vis. Sci., vol. 54, no. 7, pp.4934-4940, 2013.

[4] Delia Cabrera DeBuc, A Review of Algorithms for Segmentation of Retinal Image Data Using Optical Coherence Tomography Computer and Information Science, Artificial Intelligence, “Image Segmentation", book edited by Pei-Gee Ho, 2011. pp. 15-54.

[5] S. Sadigh, A. V. Cideciyan, A. Sumaroka, W. C. Huang, X. Luo, M. Swider, J. D. Steinberg, D. Stambolian, and and Samuel G. Jacobson, "Abnormal Thickening as well as Thinning of the Photoreceptor Layer in Intermediate Age-Related Macular Degeneration," Invest. Ophthalmol. Vis. Sci, vol. 54, pp. 1603–1612, 2013.

[6] T. Loupas and W.N. McDicken and PL Allan, "An adaptive weighted median filter for speckle suppression in medical ultrasonic images," IEEE Trans. Circuits Syst, vol. 36, pp. 129–135, 1989.

[7] Sung-jeo and Yong Hoon Lee, "Center Weighted Median Filters and Their Applications to Image enhancement," IEEE Trans. Circuits Syst, vol. 38, pp. 984–993, 1991.

[8] D. C. Fernández, H. M. Salinas, and C. A. Puliafito, "Automated detection of retinal layer structures on optical coherence tomography images," Opt. express, vol. 13, pp. 10200–10216, 2005.

[9] A. Yazdanpanah, G. Hamarneh, B. R. Smith, and and Marinko V. Sarunic, "Intra-retinal layer segmentation in optical coherence tomography using an active contour approach," Med Image Comput Comput Assist Interv, pp. 649–656, 2009.

[10] Mayer, MA, Tornow, RP, Bock, R, Hornegger, J. a. Kruse, and FE, "Automatic Nerve Fiber Layer Segmentation and Geometry Correction on Spectral Domain OCT Images Using Fuzzy C-Means Clustering," Invest. Ophthalmol. Vis. Sci, vol. 49, 2008.

[11] M. A. Mayer, J. Hornegger, C. Y. Mardin, and and Ralf P. Tornow, "Retinal nerve fiber layer segmentation on FD-OCT scans of normal subjects and glaucoma patients," Biomed Opt Express, vol. 1, pp. 1358–1383, 2010.

[12] I. Ghorbel, F. Rossant, I. Bloch, S. Tick, and M. Paques, "Automated segmentation of macular layers in OCT images and quantitative evaluation of performances," Pattern Recogn, vol. 44, pp. 81590–81603, 2011.

[13] K. A. Vermeer, J. van der Schoot, H. G. Lemij, and and J. F. de Boer, "Automated segmentation by pixel classification of retinal layers in ophthalmic OCT images," Biomed. Opt. Express, vol. 2, no. 6, pp. 1743–1756, 2011.

[14] Q. Yang, C. A. Reisman, Z. Wang, Y. Fukuma, M. Hangai, N. Yoshimura, A. Tomidokoro, M. Araie, A. S. Raza, D. C. Hood, and a. K. Chan, "Automated layer segmentation of macular OCT images using dual-scale gradient information," Opt. express, vol. 18, no. 20, pp. 21293–21307, 2010.

[15] M. D. Abramoff, K. Lee, M. Niemeijer, Wallace L. M. Alward, E. C. Greenlee, M. K. Garvin, M. Sonka, and and Young H. Kwon, "Automated Segmentation of the Cup and Rim from Spectral Domain OCT of the Optic Nerve Head," Invest. Ophthalmol. Vis. Sci, vol. 50, no. 12, pp. 5778–5784, 2009.

[16] K. Lee, M. Niemeijer, M. K. Garvin, Y. H. Kwon, M. Sonka, and and Michael D. Abramoff, "Segmentation of the Optic Disc in 3D-OCT Scans of the Optic Nerve Head," IEEE Trans. Med. Imag, vol. 29, no. 1, pp. 159–168, 2010.

[17] Q. G, L. K, D. M, G. MK, A. MD, and S. M, "Three-dimensional analysis of retinal layer texture: Identification of fluid-filled regions in SD-OCT of the macula," IEEE Trans. Med. Imag, vol. 29, no. 6, pp. 1321–1330, 2010.

[18] S. J. Chiu, X. T. Li, P. Nicholas, C. A. Toth, J. A. Izatt, and a. S. Farsiu, "Automatic segmentation of seven retinal layers in SDOCT images congruent with expert manual segmentation," Opt express, vol. 18, no. 18, pp. 19413–19428, 2010.

[19] R. Kafieh, H. Rabbani, M. D. Abramoff, and a. M. Sonka, "Intra-retinal layer segmentation of 3D optical coherence tomography using coarse grained diffusion map," Med. Image Anal, vol. 17, no. 8, pp. 907–928, 2012.

[20] Kafieh R, Rabbani H, Kermani S, "A review of algorithms for segmentation of optical coherence tomography from retina", J Med Sign Sens., Vol.3, No.1, pp.45-60, 2012.

[21] Nakano N, Hangai M, Nakanishi H, Mori S, Nukada M, Kotera Y, Ikeda HO, Nakamura H, Nonaka A, Yoshimura N., "Macular Ganglion Cell Layer Imaging in Preperimetric Glaucoma with Speckle Noise–Reduced Spectral Domain Optical Coherence Tomography", Ophthalmology, Vol. 118, No.12, pp.2414–2426, 2011.

[22] Kim M, Lee SJ, Han J, Yu SY, Kwak HW., "Segmentation error and macular thickness measurements obtained with spectral-domain optical coherence tomography devices in neovascular age-related macular degeneration", Ind J Ophthalmol., Vol.61, No.5, pp.213-217, 2013.

[23] Priyam Chatterjee and Peyman Milanfar, "Patch-Based Near-Optimal Image Denoising," IEEE Trans Med Imaging. Vol.21, No.4, pp1635-1649, 2012.

[24] Jianbing Xu, Haiyan Ou, Cuiru Sun, Po Ching Chui, Victor X. D. Yang, Edmund Y. Lam, and Kenneth K. Y. Wonga, "Wavelet domain compounding for speckle reduction in optical coherence tomography," J. Biomed. Opt., Vol.18, No.9, 096002, 2013.

[25] Markus A. Mayer, Anja Borsdorf, Martin Wagner, Joachim Hornegger, Christian Y. Mardin, and Ralf P. Tornow, "Wavelet denoising of multiframe optical coherence tomography data," Biomed. Opt. Express. 3(3), 572-589 (2012).

[26] Maciej Szkulmowski, Iwona Gorczynska, Daniel Szlag, Marcin Sylwestrzak, Andrzej Kowalczyk, and Maciej Wojtkowski, "Efficient reduction of speckle noise in Optical Coherence Tomography", Optics Express, Vol. 20, No. 2, pp.1337-1359, 2012.

[27] Bo Xiong and Zhouping Yin, "A Universal Denoising Framework with a New Impulse Detector and Nonlocal Means", IEEE Trans Biomed Eng, Vol. 21, No. 4, pp. 1663-1675, 2012.

[28] R. Maronna, R. Martin, and V. Yohar, "Robust Statistics: Theory and Methods." Chichester, U.K.: Wiley, 2006.

[29] Yazdanpanah, G. Hamarneh, B. R. Smith, and M. V. Sarunic, "Segmentation of intra-retinal layers from optical coherence tomography images using an active contour approach," IEEE Trans Med Imaging , Vol. 30, No. 2, pp. 484-496, 2011.

[30] Kalpana Saini, M. L. Dewal, and Manojkumar Rohit, "A Fast Region-Based Active Contour Model for Boundary Detection of Echocardiographic Images", J Digit Imaging. Vol. 25, No.2, pp.271–278, 2012.

[31] Mishra A. K., Fieguth P. W., and Clausi D. A., "Decoupled active contour (DAC) for boundary detection," IEEE Trans. Pattern Anal. Mach. Intell., Vol. 33, No. 2, pp.310-324, 2011.

[32] Giuseppe Papari, Nicolai Petkov, "Edge and line oriented contour detection: State of the art", Image and Vision Computing, Vol. 29, No. 2–3, pp. 79–103, 2011.

[33] Sylvain Paris, Samuel W. Hasinoff, Jan Kautz, "Local Laplacian filters: edge-aware image processing with a Laplacian pyramid." ACM Transactions on Graphics, Vol.30, No. 4, Article No. 68, 2011.

[34] Y. Y. Liu, M. Chen, H. Ishikawa, G. Wollstein, J. S. Schuman, and J. M. Rehg, "Automated macular pathology diagnosis in retinal OCT images using multi-scale spatial pyramid and local binary patterns in texture and shape encoding," Med. Image Anal., Vol. 15, No. 5, pp. 748-759, 2011.

[35] P. J. Burt and E. H. Adelson, "The Laplacian pyramid as a compact image code," IEEE Trans. Commun., Vol. 31, No. 4, pp. 532– 540, 1983.

[36] William McIlhagga, "The Canny Edge Detector Revisited", International Journal of Computer Vision, Vol. 91, No. 3, pp 251-261, 2011.

[37] Nadia Payet, Sinisa Todorovic, "SLEDGE: Sequential Labeling of Image Edges for Boundary Detection", Vol.104, No. 1, pp.15-37, 2013.

[38] Sahirzeeshan Ali, Anant Madabhushi, "An Integrated Region-, Boundary-, Shape-Based Active Contour for Multiple Object Overlap Resolution in Histological Imagery", IEEE Transactions on Medical Imaging, Vol. 31, No. 7, pp.1448-1460, 2012.

[39] Kenya Kusunose, Tomoaki Chono, Tomotsugu Tabata, Hirotsugu Yamada, Masataka Sata, "Echocardiographic image tracker with a speckle adaptive noise reduction filter for the automatic measurement of the left atrial volume curve", Eur heart j. cardiovasc. Imaging, Vol. 15, No. 5, pp. 509, 2014.

[40] W. Jeffrey Elias, Zhong A. Zheng, Paul Domer, Mark Quigg, Nader Pouratian , "Validation of connectivity-based thalamic segmentation with direct electrophysiologic recordings from human sensory thalamus", NeuroImage, Vol. 59, No. 3, pp.2025–2034, 2012.

[41] C.W. Chen, J. Luo, K.J. Parker, Image segmentation via adaptive k-mean clustering and knowledge based morphological operations with biomedical applications", IEEE Transactions on Image Processing, Vol. 7, No. 12, pp. 1673-1683, 1998.

[42] Mohandass G, Ananda Natarajan R, "layer segmentation and detection of GA and Drusen from SD-OCT images", J. theor. Appl. inf. tech., Vol. 60, No.1, pp.9-20, 2014.

[43] Mohandass G, Ananda Natarajan R & Hari Krishnan G, "Comparative analysis of optical coherence tomography retinal images using multidimensional and cluster methods.", Biomed Res- India, Vol.26 No. 2, 2015.

[44] Graham Auger, Stephen Winder, "Spectral Domain OCT: An Aid to Diagnosis and Surgical Planning of Retinal Detachments," J. of Ophthalmology, Vol. 2011. Article ID 725362, 2011.

[45] P. Jindahra, T. R. Hedges, C. E. Mendoza-Santiesteban, G. T. Plant, "Optical coherence tomography of the retina: applications in neurology," Curr. Opin. Neurol., Vol. 23, No. 1, pp. 16–23, 2010.

[46] S. Saidha, S. B. Syc, M. A. Ibrahim, C. Eckstein, C. V. Warner, S. K. Farrell, J. D. Oakley, M. K. Durbin, S. A. Meyer, L. J. Balcer, E. M. Frohman, J. M. Rosenzweig, S. D. Newsome, J. N. Ratchford, Q. D. Nguyen, and P. A. Calabresi, "Primary retinal pathology in multiple sclerosis as detected by optical coherence tomography," Brain, Vol. 134, No. 11, pp. 518–533, 2011.

[47] Kijas JW, Cideciyan AV, Aleman TS, Pianta MJ, Pearce-Kelling SE, Miller BJ, Jacobson SG, Aguirre GD, Acland GM, "Naturally occurring rhodopsin mutation in the dog causes retinal dysfunction and degeneration mimicking human dominant retinitis pigmentosa", Proc. Natl. Acad. Sci. U S A., Vol. 99, No. 9, pp.6328-6333, 2002.

[48] G. Huber, S. C. Beck, C. Grimm, A. Sahaboglu-Tekgoz, F. Paquet-Durand, A. Wenzel, P. Humphries, T. M. Redmond, M. W. Seeliger, and M. D. Fischer, "Spectral domain optical coherence tomography in mouse models of retinal degeneration," Invest. Ophthalmol. Vis. Sci., Vol.50, No. 12, pp.5888–5895, 2009.

[49] Y. Muraoka, H. O. Ikeda, N. Nakano, M. Hangai, Y. Toda, K. Okamoto-Furuta, H. Kohda, M. Kondo, H. Terasaki, A. Kakizuka, and N. Yoshimura, "Real-time imaging of rabbit retina with retinal degeneration by using spectral-domain optical coherence tomography", PloS One, 2012.

[50] Randa S. Eshaqa, William S. Wrightb, Norman R. Harrisa,"Oxygen delivery, consumption, and conversion to reactive oxygen species in experimental models of diabetic retinopathy", Redox biology, vol.2, pp. 661-666, 2014.

[51] Olena Puzyeyeva, Wai Ching Lam, John G. Flanagan, Michael H. Brent, Robert G. Devenyi, Mark S. Mandelcorn, Tien Wong, and Christopher Hudson, "High-Resolution Optical Coherence Tomography Retinal Imaging: A Case Series Illustrating Potential and Limitations", Journal of Ophthalmology, Vol. 2011, Article ID 764183, 2011.

[52] Tae Joong Eom, Yeh-Chan Ahn, Chang-Seok Kim, and Zhongping Chen, "Calibration and characterization protocol for spectral-domain optical coherence tomography using fiber Bragg gratings," J. Biomed. Opt., Vol. 16, No.3, 030501-3, 2011.

[53] C. Sull, L. N. Vuong, and L. L. Price, "Comparison of spectral/Fourier domain optical coherence tomography instruments for assessment of normal macular thickness," Retina, Vol. 30, No. 2, pp. 235–245, 2010.